JOURNAL OF COMPUTATIONAL PHYSICS **65**, 253–272 (1986)

3D Nonlinear MHD Calculations Using Implicit and Explicit Time Integration Schemes*

L. GARCIA, H. R. HICKS, B. A. CARRERAS, L. A. CHARLTON, AND J. A. HOLMES

Oak Ridge National Laboratory, Oak Ridge, Tennessee 37831

Received May 1, 1985; revised October 23, 1985

A computer code (KITE) that solves a reduced set of magnetohydrodynamic (MHD) equations with diamagnetic and thermal force effects included has been constructed. It can use two different time integration schemes. A mostly-explicit time integration scheme is shown to be efficient for the nonlinear phase of tearing mode turbulence where numerical stability demands a small timestep. However, for linear calculations, or nonlinear ones in which the level of turbulence is low, a mostly-implicit approach is seen to be more efficient. The two numerical schemes yield the same solutions. Nonlinear MHD calculations in which the solutions are represented by a finite Fourier series allow one to study the dependence of the nonlinear solution on its permitted harmonic content. It is seen that for the 3-dimensional (3D), nonlinear, tearing mode disruption problem, the refinement of the solution by the addition of more modes leads to further destabilization. This contrasts to the rippling mode problem, in which the addition of modes is stabilizing. For the latter, a finite number of modes yields a converged solution that is a saturated state. This contrasting behavior reflects the basic physical mechanism of the nonlinear interaction in each case and not the particular numerical scheme used for the calculations.

1. INTRODUCTION

The resistive MHD model has been used in formulating possible explanations for disruptions and enhanced transport in tokamak discharges. For many of these phenomena, the basic physics can be understood using the reduced set of MHD equations [1], derived from the full resistive MHD equations with the standard tokamak (inverse aspect ratio) ordering and the assumption of a low-β plasma. This reductions in the number of equations and the consequent elimination of the fast Alfvén waves allow the efficient study of 3-dimensional (3D) nonlinear evolution. Numerous such calculations that have led to a better understanding of experimental tokamak data have been carried out in recent years [2].

In the first studies of nonlinear resistive MHD, we extensively used the code RSF [3, 4], which solves the reduced set of equations in a periodic plasma cylinder. The resistivity evolution is included through an electron heat conduction equation. The

---

* Research sponsored by the Office of Fusion Energy, under Contract DE-AC05-84OR21400 with Martin Marieta Energy Systems, Inc. The U. S. Government's right to retain a nonexclusive royalty-free license in and to the copyright covering this paper, for governmental purposes, is acknowledged.

0021-9991/86 $3.00

numerical scheme is explicit, except for convective and resistive diffusion terms. This approach is optimized for the nonlinear phase of tearing mode calculations. However, this scheme is not as efficient for other calculations in which it may require an unnecessarily small timestep. In addition, RSF is a pure resistive MHD code and does not include the effects of viscosity, diamagnetism [5], and thermal force [6].

In this paper we describe a new code, KITE, that has been devised to study these effects and to relax the timestep limitations of RSF. This nonlinear code includes the density and temperature evolution, together with the magnetic flux and momentum balance equations. Two time integration schemes have been developed: one, "mostly-explicit," is a generalization of the RSF scheme, while the other, "mostly-implicit," uses a fully implicit scheme for the linear terms and is more efficient in the linear regime. It is also more efficient in nonlinear calculations when the saturation level of the modes is low and the physical parameters force the explicit scheme timestep to be very small. Both schemes, however, yield the same solutions. Both RSF and KITE represent solutions using finite difference in minor radius and a Fourier series expansion in the two periodic coordinates.

We also consider two physics examples to illustrate the strengths of each numerical scheme. The saturation of resistivity-gradient-driven rippling modes [7] is due to the balance between parallel diffusion and the turbulent radial diffusion of the resistivity perturbations induced by nonlinear convection. Due to its intrinsic turbulent character, this saturation cannot be observed numerically when an insufficient number of modes are included in the computation. Increasing the number of modes in the representation of the solution increases the stabilizing effect. Convergence studies with respect to the number of modes yield the converged saturated state. On the other hand, in a disruption caused by the nonlinear interaction of tearing modes, the picture is just the opposite. The final phase of the disruption is characterized by nonstationary, growing turbulence [4, 8]. Numerically, a nonphysical, saturated state can be observed when a low number of modes is included in the calculation [4, 9]. However, this is not a converged solution to the problem. As the number of modes numerically represented in the calculation is increased, more and more modes are excited, and low-m modes are further destabilized. So, unlike the rippling mode case, the addition of modes is destabilizing. The number of modes required for a converged solution continues to increase as the solution evolves with time. Conversely, a calculation using a fixed number of modes yields a valid solution only up to a particular time. This contrasting behavior reflects the basic physics mechanism of the nonlinear interaction and is independent of the numerical scheme used for the calculation.

The equations used in the code are discussed in Section 2. Section 3 is devoted to the description and comparison of the numerical schemes, while Section 4 describes the convergence studies, with special emphasis on convergence with respect to the number of modes. Finally, Section 5 contains the conclusions.

2. EQUATIONS

The equations used in KITE are an extended version of the reduced set of resistive MHD equations [1], including diamagnetic and electron temperature effects. The addition of diamagnetic effects has been discussed in [5, 10, 11]. The effect of the thermal force and an equation for the electron temperature, derived from the two-fluid MHD equations [6, 12], have been included. The equations are solved in cylindrical geometry using an (r, θ, ζ) coordinate system, where r $(0 < r < 1)$ is the radial coordinate normalized to the radius of the cylinder a, θ $(0 < \theta < 2\pi)$ is the poloidal angle, and ζ $(0 < \zeta < 2\pi)$ is an angle-like coordinate such that $\zeta = 2\pi Z/L$, where Z is the coordinate along the axis of the cylinder of length L. For analogy with toroidal geometry, we shall refer to ζ as the toroidal angle, the unit vector $\hat{\zeta}$ in that direction as the toroidal direction, and $R = L/2\pi$ as the major radius of the torus. In dimensionless form, the equations are

$$\frac{\partial \Psi}{\partial t} = -\mathbf{v}_\perp \cdot \nabla_\perp \Psi - \frac{\partial \Phi}{\partial \zeta} + \frac{1}{S}(\eta J_\zeta - E_\zeta^{\omega})$$

$$- (\omega_{*e} T_e - \omega_{*i} T_i) - \frac{1}{\rho} \nabla_\parallel \rho - (1 + \alpha)\, \omega_{*e} \nabla_\parallel T_e, \tag{1a}$$

$$\frac{\partial U}{\partial t} = -\mathbf{v}_\perp \cdot \nabla_\perp U - \frac{1}{2} \hat{\zeta} \cdot [\nabla \rho \times \nabla v_\perp^2] - \nabla_\parallel J_\zeta + \frac{1}{R_u} \nabla_\perp^2 U$$

$$+ \omega_{*i} \nabla_\perp \cdot ([(\nabla_\perp \rho \times \hat{\zeta}) \cdot \nabla_\perp]\, \nabla_\perp \Phi), \tag{1b}$$

$$\frac{\partial \rho}{\partial t} = -\mathbf{v}_\perp \cdot \nabla_\perp \rho + \frac{1}{\omega_{cy}} \nabla_\parallel J_\zeta + \frac{1}{R_\rho} \nabla_\perp^2 (\rho - \rho^{\mathrm{eq}}), \tag{1c}$$

$$\frac{\partial T_e}{\partial t} = -\mathbf{v}_\perp \cdot \nabla_\perp T_e + \frac{1}{\rho} \nabla_\parallel (\bar{\chi}_\parallel \rho \nabla_\parallel T_e) + \bar{\chi}_\perp \nabla_\perp^2 (T_e - T_e^{\mathrm{eq}})$$

$$+ \frac{1}{\omega_{cy}} \frac{1}{\rho} \left[J_\zeta \nabla_\parallel T_e + \frac{2}{3}(1 + \alpha)\, T_e \nabla_\parallel J_\zeta - \frac{2}{3} \frac{1}{\rho} J_\zeta T_e \nabla_\parallel \rho \right], \tag{1d}$$

and

$$\eta = T_e^{-3/2}, \tag{1e}$$

where Ψ is the poloidal magnetic flux function, related to the magnetic field by $\mathbf{B} = \hat{\zeta} - \varepsilon \nabla \Psi \times \hat{\zeta}$, with $\varepsilon = 2\pi a/L$ the inverse aspect ratio of the cylinder; J_ζ is the toroidal component of the current density, given by $J_\zeta = \nabla_\perp^2 \Psi$; η, ρ, and T_e are, respectively, the resistivity, mass density, and electron temperature, normalized to their magnetic axis values; Φ is the velocity stream function, related to the poloidal fluid velocity by $\mathbf{v}_\perp = \nabla \Phi \times \hat{\zeta}$; U is the toroidal component of the vorticity, given by $U = \nabla \cdot (\rho \nabla_\perp \Phi)$. Here, $\perp$ denotes perpendicular to $\hat{\zeta}$, and $\nabla_\parallel = \partial/\partial\zeta - (\nabla \Psi \times \hat{\zeta}) \cdot \nabla$ is the gradient parallel to the magnetic field. The time t is normalized to the poloidal

Alfvén time $\tau_{H\rho} = R/v_A$, where v_A is the poloidal Alfvén velocity $v_A = B_\zeta/[\mu_0 m_i n_i(0)]^{1/2}$. The magnetic field is normalized to the constant toroidal field. The dimensionless parameters appearing in the equations are S $(= \tau_R/\tau_{H\rho})$, the ratio of the resistive time to the poloidal Alfvén time, where $\tau_R = \mu_0 a^2/\eta(0)$; ω_{*e} $[= \tau_{Hp} T_e(0)/ea^2 B_\zeta]$; and ω_{*i} $[= -\tau_{Hp} T_i(0)/Zea^2 B_\zeta]$, the electron and ion diamagnetic frequencies, respectively, normalized to τ_{Hp}^{-1}; ω_{cy} $(= \omega_{ci}\tau_{Hp})$, where ω_{ci} is the ion cyclotron frequency; R_u $(= -10\omega_{ci}\tau_i/3\omega_{*i})$, the coefficient of the perpendicular viscosity, where τ_i is the ion collisional time; R_ρ, the perpendicular mass diffusion coefficient; $\bar{\chi}_\parallel$ $(= 2\tau_{Hp}\kappa_\parallel^e/3R^2 n_e)$, and $\bar{\chi}_\perp$ $(= 2\tau_{Hp}\kappa_\perp^e/3a^2 n_e)$, the parallel and perpendicular electron heat conductivities, respectively, while α has the value 0.71 [12].

The code allows the study of different physical phenomena, depending on which terms are included in the evolution equations. Tearing modes can be studied with only the magnetic flux and vorticity equations [13] and taking ρ, T_e, and η constant in time. The introduction of self-consistent resistivity evolution through the electron temperature equation, using the Spitzer relation between resistivity and electron temperature $(\eta = T^{-3/2})$, allows the calculation of resistivity-driven processes, such as turbulence due to rippling modes [7, 14]. Diamagnetic effects on the stability of resistive modes can be studied by adding the density equation and introducing the density gradient terms in the other equations [5]. Finally, the equations can also include thermal force effects through the temperature gradient term.

All the fields can be represented by two components, equilibrium and perturbation:

$$f(r, \theta, \zeta) = f^{\mathrm{eq}}(r) + \tilde{f}(r, \theta, \zeta), \tag{2}$$

where the perturbation is written as an expansion in sines and cosines,

$$\tilde{f}(r, \theta, \zeta) = \sum_{m,n} [f^c_{mn} \cos(m\theta + n\zeta) + f^s_{mn} \sin(m\theta + n\zeta)]. \tag{3}$$

The equilibrium is an exact, steady state, velocity-free solution of Eq. (1). For such a state, $\Phi = U = 0$. Thus, Eq. (1) yields

$$\frac{\partial \Psi^{\mathrm{eq}}}{\partial t} = \frac{1}{S}(\eta J_\zeta^{\mathrm{eq}} - E_\zeta^\omega), \tag{4a}$$

and

$$\frac{\partial U^{\mathrm{eq}}}{\partial t} = \frac{\partial \rho^{\mathrm{eq}}}{\partial t} = \frac{\partial T_e^{\mathrm{eq}}}{\partial t} = 0. \tag{4b}$$

From the momentum balance equation,

$$\nabla_\parallel J_\zeta^{\mathrm{eq}} = 0, \tag{5}$$

which implies that J_ζ^{eq} and, therefore, Ψ^{eq} are only functions of r. To avoid the resistive decay of the equilibrium magnetic flux, Eq. (4a), we can set

$$\eta^{\text{eq}}(r) = [J_\zeta^{\text{eq}}(r)]^{-1} E_\zeta^{\omega}. \tag{6}$$

An equilibrium can be specified by fixing $\Psi^{\text{eq}}(r)$, which in turn is given by the safety factor profile q through the relation

$$\frac{d\Psi^{\text{eq}}}{dr} = -\frac{r}{q(r)}. \tag{7}$$

The equilibrium electron temperature is also a function of r only and is related to the resistivity through the Spitzer relation

$$T_e^{\text{eq}} = (\eta^{\text{eq}})^{-2/3}, \tag{8}$$

while the ion temperature and equilibrium mass density have specified profiles. For the calculations shown here, $\omega_{*i} = 0$, and the equilibrium mass density is also a function of r only and has been parameterized as follows:

$$\rho^{\text{eq}}(r) = \left(1 - \frac{1}{2}\rho_0\right)(1 - r^2)^2 + \frac{1}{2}\rho_0,$$

where ρ_0 is a parameter that we have taken to be 1 or 0.5. Thus, only two profiles, namely q and ρ^{eq}, are needed to specify an equilibrium.

The boundary conditions are that the radial magnetic field and velocity are zero at the conducting wall. That is, Ψ and Φ, as well as the perturbation of ρ and T_e, vanish at the cylindrical wall:

$$\Psi(1, \theta, \zeta) = \Phi(1, \theta, \zeta) = 0, \tag{9a}$$

$$\tilde{\rho}(1, \theta, \zeta) = \tilde{T}_e(1, \theta, \zeta) = 0. \tag{9b}$$

To perform a stability calculation, it is necessary to add a small ζ- and/or θ-dependent perturbation to the equilibrium. Depending on the characteristics of the problem, the magnetic flux Ψ or the velocity field Φ is initially perturbed. For a tearing mode calculation, since it is dominated by a magnetic mode, we initially set $\Phi_{m,n} = 0$, and an initial $\tilde{\Psi}$ is given by

$$\tilde{\Psi} = -\left(\frac{W_{m,n}^{\text{I}}}{4}\right)^2 \frac{r^m(1-r)}{r_s^m(1-r_s)} \frac{2}{1 + e^{10(-1+r/r_s)}} \frac{r_s q'(r_s)}{q(r_s)^2} \cos(m\theta + n\zeta), \tag{10}$$

where r_s is the radius of the singular surface, $q(r_s) = m/n$, $q' = dq/dr|_{r_s}$, and W_{mn}^{I} is the approximate initial island width. For a rippling mode calculation, since it is dominated by an electrostatic mode, we initially set $\tilde{\Psi}_{mn} = 0$ and

$$\Phi = \begin{cases} W_{m,n}^{\text{I}} \left(\dfrac{r}{r_s}\right)^m \exp\left[-\dfrac{(r - \bar{r}_s)^2}{\Gamma}\right] \sin(m\theta + n\zeta) & r \leqslant r_s, \\ W_{m,n}^{\text{I}} \left(\dfrac{1-r}{1-r_s}\right) \exp\left[-\dfrac{(r - \bar{r}_s)^2}{\Gamma}\right] \sin(m\theta + n\zeta) & r > r_s; \end{cases} \tag{11}$$

where $\bar{r}_s = r_s + \Gamma$. Γ is an arbitrary parameter that gives the desired width in radius of the initial perturbation. One or several modes of the same helicity can be initialized by using Eqs. (10) or (11) in order to study a 2-dimensional (2D) single-helicity time evolution. Alternately, by initializing several modes of different helicities (m/n) one can perform a 3D calculation. The solution is, in general, independent of the radial dependence of the initial perturbation as long as the perturbation is sufficiently small. The precise choice of the initial perturbation is made in order to approach the linear solution as quickly as possible.

From Eq. (1), when $\omega_{*i} = 0$, the energy-balance equation is

$$\frac{dE_{\mathrm{K}}}{dt} + \frac{dE_{\mathrm{M}}}{dt} + \frac{dE_{\mathrm{T}}}{dt} = -Q_{\mathrm{J}} + Q_{\mathrm{P}} - Q_{\mathrm{V}} - Q_{\mathrm{Ve}} - Q_{\mathrm{D}} - Q_{\mathrm{T}}, \tag{12}$$

where E_{K}, E_{M}, and E_{T} are the kinetic, magnetic, and thermal energies of the plasma. They are given by

$$E_{\mathrm{K}} = \frac{1}{2} \int d^3\mathbf{r} \rho \, |\nabla_\perp \Phi|^2, \tag{13}$$

$$E_{\mathrm{M}} = \frac{1}{2} \int d^3\mathbf{r} \, |\nabla_\perp \Psi|^2, \tag{14}$$

$$E_{\mathrm{T}} = \frac{3}{4} \frac{\beta_{0e}}{\varepsilon^2} \int d^3\mathbf{r} \rho T_e, \tag{15}$$

where

$$\beta_{0e} = 2\omega_{cy}\omega_{*e} = \frac{n_e(0)\, T_e(0)}{(1/2\mu_0)\, B_\zeta^2}.$$

The energy source is due to the applied toroidal electric field and is given by

$$Q_P = \frac{1}{S} E_\zeta^\omega \int d^3\mathbf{r} J_\zeta = \frac{1}{S} E_\zeta^\omega \int d\mathbf{n} \cdot \nabla \Psi. \tag{16}$$

Finally, there are several sinks of energy,

$$Q_{\mathrm{J}} = \frac{1}{S} \int d^3\mathbf{r} \eta J_\zeta^2, \tag{17}$$

$$Q_{\mathrm{V}} = \frac{1}{R_u} \int d^3\mathbf{r} \Phi \nabla_\perp^2 U, \tag{18}$$

$$Q_{\mathrm{Ve}} = \frac{1}{2\omega_{cy}} \int d^3\mathbf{r} v_\perp^2 \nabla_\parallel J_\zeta, \tag{19}$$

$$Q_{\mathrm{D}} = \frac{1}{R_\rho} \left[\frac{1}{2} \int d^3\mathbf{r} v_\perp^2 \nabla_\perp^2 (\rho - \rho^{eq}) - \frac{3}{4} \frac{\beta_{0e}}{\varepsilon^2} \int T_e \nabla_\perp^2 (\rho - \rho^{eq}) \right], \tag{20}$$

$$Q_{\mathrm{T}} = -\frac{3}{4} \frac{\beta_{0e}}{\varepsilon^2} \bar{\chi}_\perp \int d^3\mathbf{r} \rho \nabla_\perp^2 (T_e - T_e^{eq}), \tag{21}$$

where Q_J is the rate of energy dissipation due to Joule heating, Q_V and Q_{Ve} are the rates of energy dissipation due to viscosity, and Q_D and Q_T are the rates of energy dissipation due to diffusion in density and temperature, respectively. Each of the energy terms can be expressed as the sum of individual mode energies; for example,

$$E_M = \sum_{m,n} E_M(m;n), \tag{22}$$

where

$$E_M(m;n) = (\tfrac{1}{2} + \tfrac{1}{2}\,\delta_{m0}\,\delta_{n0}) \int d^3\mathbf{r}\,|\nabla_\perp \Psi_{m,n}|^2. \tag{23}$$

In the implementations of Eq. (1) to be described shortly, the energy-balance equation (Eq. (12)) is not part of the dynamics. Therefore, as a diagnostic it provides a test for numerical error. We define a total cumulative energy-balance error of

$$\Delta E_T = E_K + E_M + E_T - E_K^I - E_M^I - E_T^I + \int_0^t dt(Q_J - Q_P + Q_V + Q_{Ve} + Q_D + Q_T), \tag{24}$$

where the right side is obtained by numerically evaluating Eqs. (13) to (21) and E^I denotes the energy at the beginning of the calculation. This will contain Δr and Δt truncation error, both from the dynamic solution and from the evaluation of Eq. (24) itself.

The energy conservation equation is not only useful for testing the numerics in the evolution, but, more important, is a guide to which terms in the equations are related to the physical effects being studied.

The instantaneous growth rates and real frequencies, defined for each scalar field by

$$\gamma = \frac{\int r\,dr[f^c_{mn}(t+\Delta t)^2 + f^s_{mn}(t+\Delta t)^2 - f^c_{mn}(t)^2 - f^s_{mn}(t)^2]}{\Delta t \int r\,dr[f^c_{mn}(t+\Delta t)^2 + f^s_{mn}(t+\Delta t)^2 + f^c_{mn}(t)^2 + f^s_{mn}(t)^2]}, \tag{25}$$

$$\omega_r = \frac{\int r\,dr[f^s(t+\Delta t)\,f^c(t) - f^c(t+\Delta t)\,f^s(t)]}{\Delta t \int r\,dr[f^c(t)^2 + f^s(t)^2]}, \tag{26}$$

are useful diagnostics for describing the mode behavior during the evolution. They allow us to determine energy flows and saturation and can be used also in numerical tests for convergence.

3. NUMERICAL SCHEMES

Two different methods are used to solve the equations. Their relative efficiency depends on the type of calculation. Both methods use a representation that is finite difference in r and spectral in θ and ζ.

Each scalar field is written as an expansion in sines and cosines (Eq. (3)). The resulting "modes" are functions of r represented on a finite-difference grid. First and second radial derivatives are performed with three-point finite-difference formulas that allow unequal spacing. Derivatives in θ and ζ are performed analytically. All quantities are stored in spectral form (Eq. (3)) and are never transformed to a finite-difference grid in θ or ζ. The convolutions are performed analytically, rather than by using fast Fourier transforms.

In addition to specifying the radial grid points, it is necessary (for nonlinear calculations) to choose a finite set of modes ($(m; n)$ pairs) to be included in the expansions (Eq. (3)). We have developed procedures for selecting relatively optimal sets of modes [3]. A few dominant modes are chosen, based on the physics of the problem to be studied. Then, a sequence of mode sets can be obtained from successive application of the nonlinear couplings [3]. Thus, different physics problems tend to be calculated with different numbers of modes, as can be seen in the figures. For the calculations shown here, the dominant modes fall in a band in $(m; n)$ space. However, convergence with respect to mode truncation must be demonstrated by varying the choice of modes included.

The difference between the two schemes presented here lies in the treatment of the linear terms and the order of accuracy of the time integration. The following sections present a detailed description of both schemes.

3.1. *The Mostly Explicit Scheme*

In this scheme, the time integration is second-order accurate and, except for the diffusive terms, is explicit. The technique was first described in [3] for only the Ψ and U equations.

For advancing Eqs. (1) from t to $t + \Delta t$, first U and ρ are advanced to $t + \Delta t/2$ using

$$\begin{aligned}\frac{U^{t+\Delta t/2} - U^t}{\Delta t/2} = {} & -\nabla_\| \tilde{J}_\zeta^t + [U^t, \Phi^t] + \frac{1}{R_u} \nabla_\perp^2 U^{t+\Delta t/2} \\ & + \frac{1}{2}\left[\tilde{\rho}^t, (\nabla_r \Phi^t)^2 + (\nabla_\theta \Phi^t)^2\right] - \omega_{*i} \frac{1}{r} \nabla_r \left[r \frac{d\rho^{\text{eq}}}{dr} \nabla_r (\nabla_\theta \Phi^t) \right] \\ & + \omega_{*i} \boldsymbol{\nabla}_\perp \cdot ([(\boldsymbol{\nabla}_\perp \tilde{\rho}^t \times \hat{\zeta}) \cdot \boldsymbol{\nabla}_\perp] \boldsymbol{\nabla}_\perp \Phi^t),\end{aligned} \tag{27}$$

$$\begin{aligned}\frac{\rho^{t+\Delta t/2} - \rho^t}{\Delta t/2} = {} & -\frac{d\rho^{\text{eq}}}{dr} \nabla_\theta \Phi^t + [\tilde{\rho}^t, \Phi^t] + \frac{1}{\omega_{cy}} \nabla_\| \tilde{J}_\zeta^t \\ & + \frac{1}{R_\rho} \nabla_\perp^2 \tilde{\rho}^{t+\Delta t/2}.\end{aligned} \tag{28}$$

Next, Ψ and T_e are advanced:

$$\begin{aligned}\frac{\Psi^{t+\Delta t/2}-\Psi^{t}}{\Delta t/2}={}&-\left(\frac{\partial}{\partial\zeta}-\frac{r}{q}\nabla_\theta\right)\Phi^{t+\Delta t/2}+[\tilde{\Psi}^{t},\Phi^{t+\Delta t/2}]\\&+\eta^{\mathrm{eq}}\tilde{J}_\zeta^{t+\Delta t/2}+\tilde{\eta}^{t}J_\zeta^{\mathrm{eq}}+\tilde{\eta}^{t}\tilde{J}_\zeta^{t}\\&-(\omega_{*e}T_e^{t}-\omega_{*i}T_i)\frac{1}{\rho_{00}^{t+\Delta t/2}}\nabla_\parallel\tilde{\rho}^{t+\Delta t/2}-(1+\alpha)\,\omega_{*e}\tilde{T}_e^{t},\end{aligned}\tag{29}$$

$$\begin{aligned}\frac{T_e^{t+\Delta t/2}-T_e^{t}}{\Delta t/2}={}&-\frac{dT_e^{\mathrm{eq}}}{dr}\nabla_\theta\Phi^{t+\Delta t/2}+[\tilde{T}_e^{t},\Phi^{t+\Delta t/2}]\\&+\bar{\chi}_\perp\nabla_\perp^2\tilde{T}_e^{t+\Delta t/2}+\frac{1}{\rho_{00}^{t+\Delta t/2}}\bar{\chi}_\parallel\nabla_\parallel[\rho^{t+\Delta t/2}\nabla_\parallel\tilde{T}_e^{t}]\\&+\frac{1}{\omega_{ci}}\frac{1}{\rho_{00}^{t+\Delta t/2}}\left[J_\zeta^{t}\nabla_\parallel\tilde{T}_e^{t}+\frac{2}{3}(1+\alpha)\,\tilde{T}_e^{t}\nabla_\parallel\tilde{J}_\zeta^{t}-\frac{2}{3}\frac{1}{\rho_{00}^{t+\Delta t/2}}J_\zeta^{t}T_e^{t}\nabla_\parallel\tilde{\rho}^{t+\Delta t/2}\right],\end{aligned}\tag{30}$$

where $\Phi^{t+\Delta t/2}$ is obtained by solving $U^{t+\Delta t/2}=\nabla\cdot(\rho_{00}^{t+\Delta t/2}\nabla_\perp\Phi^{t+\Delta t/2})$, and $\tilde{\eta}=-(3/2)\,\eta^{eq}\tilde{T}_e/T_e^{\mathrm{eq}}$.

Finally, a time-centered solution is obtained by

$$\begin{aligned}\frac{U^{t+\Delta t}-U^{t}}{\Delta t}={}&-\nabla_\parallel\tilde{J}_\zeta^{t+\Delta t/2}+[U^{t+\Delta t/2},\Phi^{t+\Delta t/2}]+\frac{1}{R_u}\nabla_\perp^2U^{t+\Delta t/2}\\&+\tfrac{1}{2}[\tilde{\rho}^{t+\Delta t/2},(\nabla_r\Phi^{t+\Delta t/2})^2+(\nabla_\theta\Phi^{t+\Delta t/2})^2]\\&-\omega_{*i}\frac{1}{r}\nabla_r\left[r\frac{d\rho^{\mathrm{eq}}}{dr}\nabla_r(\nabla_\theta\Phi^{t+\Delta t/2})\right]\\&+\omega_{*i}\boldsymbol{\nabla}_\perp\cdot([(\boldsymbol{\nabla}_\perp\tilde{\rho}^{t+\Delta t/2}\times\hat{\zeta})\cdot\nabla_\perp]\,\boldsymbol{\nabla}_\perp\Phi^{t+\Delta t/2}),\end{aligned}\tag{31}$$

$$\begin{aligned}\frac{\rho^{t+\Delta t}-\rho^{t}}{\Delta t}={}&-\frac{d\rho^{\mathrm{eq}}}{dr}\nabla_\theta\Phi^{t+\Delta t/2}+[\tilde{\rho}^{t+\Delta t/2},\Phi^{t+\Delta t/2}]\\&+\frac{1}{\omega_{ci}}\nabla_\parallel\tilde{J}_\zeta^{t+\Delta t/2}+\frac{1}{R_\rho}\nabla_\perp^2\tilde{\rho}^{t+\Delta t/2},\end{aligned}\tag{32}$$

$$\begin{aligned}\frac{\Psi^{t+\Delta t}-\Psi^{t}}{\Delta t}={}&-\left(\frac{\partial}{\partial\zeta}-\frac{r}{q}\nabla_\theta\right)\Phi^{t+\Delta t/2}+[\tilde{\Psi}^{t+\Delta t/2},\Phi^{t+\Delta t/2}]\\&+\eta^{\mathrm{eq}}\tilde{J}_\zeta^{t+\Delta t/2}+\tilde{\eta}^{t+\Delta t/2}J_\zeta^{\mathrm{eq}}+\tilde{\eta}^{t+\Delta t/2}\tilde{J}_\zeta^{t+\Delta t/2}\\&-(\omega_{*e}T_e^{t+\Delta t/2}-\omega_{*i}T_i)\frac{1}{\rho_{00}^{t+\Delta t/2}}\nabla_\parallel\tilde{\rho}^{t+\Delta t/2}-(1+\alpha)\,\omega_{*e}\tilde{T}_e^{t+\Delta t/2},\end{aligned}\tag{33}$$

and

$$\begin{aligned}\frac{T_e^{t+\Delta t}-T_e^t}{\Delta t} &= -\frac{dT_e^{\mathrm{eq}}}{dr}\nabla_\theta \Phi^{t+\Delta t/2}+[\tilde{T}_e^{t+\Delta t/2}, \Phi^{t+\Delta t/2}]\\ &\quad +\bar{\chi}_\perp \nabla_\perp^2 \tilde{T}_e^{t+\Delta t/2}+\frac{1}{\rho_{00}^{t+\Delta t/2}}\bar{\chi}_\parallel \nabla_\parallel [\rho^{t+\Delta t/2}\nabla_\parallel \tilde{T}_e^{t+\Delta t/2}]\\ &\quad +\frac{1}{\omega_{cy}}\frac{1}{\rho_{00}^{t+\Delta t/2}}\left[J_\zeta^{t+\Delta t/2}\nabla_\parallel \tilde{T}_e^{t+\Delta t/2}+\frac{2}{3}(1+\alpha)\, T_e^{t+\Delta t/2}\nabla_\parallel \tilde{J}_\zeta^{t+\Delta t/2}\right.\\ &\quad \left. -\frac{2}{3}\frac{1}{\rho_{00}^{t+\Delta t/2}} J_\zeta^{t+\Delta t/2}\, T_e^{t+\Delta t/2}\nabla_\parallel \tilde{\rho}^{t+\Delta t/2}\right]. \end{aligned} \tag{34}$$

Here,

$$\nabla_\theta \equiv \frac{1}{r}\frac{\partial}{\partial\theta}, \qquad \nabla_r \equiv \frac{\partial}{\partial r}, \qquad \nabla_\perp^2 = \frac{1}{r^2}\frac{\partial^2}{\partial\theta^2}+\frac{1}{r}\frac{\partial}{\partial r}\left(r\frac{\partial}{\partial r}\right),$$

$$[a, b] \equiv \nabla_\theta a \nabla_r b - \nabla_r a \nabla_\theta b,$$

and

$$\nabla_\parallel \tilde{J} = \left(\frac{\partial}{\partial\zeta}-\frac{r}{q}\nabla_\theta\right)\tilde{J}-\frac{df^{\mathrm{eq}}}{dr}\nabla_\theta \tilde{\Psi}-[\tilde{\Psi}, \tilde{J}], \tag{35}$$

with $\tilde{\Psi}$ evaluated at t in Eqs. (27) to (30) and at $t+\Delta t/2$ in Eqs. (31) to (34). A procedure to reduce the timestep whenever a numerical instability becomes significant has been developed [4]. In effect, this tolerates situations that are at the numerical instability boundary. This is desirable in a calculation in which the physical solutions are growing. To verify that a numerical instability is not affecting the solution, it is necessary to compare calculations performed with different timesteps or different numerical schemes.

3.2. *The Mostly Implicit Scheme*

In this scheme the nonlinear terms are explicit and first-order accurate in time, and the linear terms are treated implicitly, with the order of accuracy dependent on a parameter W:

$$U^{t+\Delta t}-W\,\Delta t T_1^{t+\Delta t}=U^t-W\,\Delta t T_1^t+\Delta t S_1, \tag{36a}$$

$$\rho^{t+\Delta t}-W\,\Delta t T_2^{t+\Delta t}=\rho^t-W\,\Delta t T_2^t+\Delta t S_2, \tag{36b}$$

$$\Psi^{t+\Delta t}-W\,\Delta t T_3^{t+\Delta t}=\Psi^t-W\,\Delta t T_3^t+\Delta t S_3, \tag{36c}$$

$$T_e^{t+\Delta t}-W\,\Delta t T_4^{t+\Delta t}=T_e^t-W\,\Delta t T_4^t+\Delta t S_4, \tag{36d}$$

where

$$T_1 = -\partial_\parallel \tilde{J}_\zeta + \frac{1}{R_u}\nabla_\perp^2 U - \omega_{*i}\frac{1}{r}\nabla_r\left[r\frac{d\rho^{\mathrm{eq}}}{dr}\nabla_r(\nabla_\theta \Phi)\right], \tag{37}$$

$$T_2 = -\frac{d\rho^{\mathrm{eq}}}{dr}\nabla_\theta \Phi + \frac{1}{\omega_{cy}}\partial_\parallel \tilde{J}_\zeta + \frac{1}{R_\rho}\nabla_\perp^2 \tilde{\rho}, \tag{38}$$

$$\begin{aligned} T_3 = &-\left(\frac{\partial}{\partial\zeta} - \frac{r}{q}\nabla_\theta\right)\Phi + \eta^{\mathrm{eq}}\tilde{J}_\zeta + J_\zeta^{\mathrm{eq}}\tilde{\eta} \\ &-(\omega_{*e}T_e^{\mathrm{eq}} - \omega_{*i}T_i)\frac{1}{\rho^{\mathrm{eq}}}\partial_\parallel \tilde{\rho} - (1+\alpha)\,\omega_{*e}\partial_\parallel \tilde{T}_e, \end{aligned} \tag{39}$$

$$\begin{aligned} T_4 = &-\frac{dT_e^{\mathrm{eq}}}{dr}\nabla_\theta \Phi + \bar{\chi}_\perp \nabla_\perp^2 \tilde{T}_e + \frac{1}{\rho^{\mathrm{eq}}}\bar{\chi}_\parallel\left(\frac{\partial}{\partial\zeta} - \frac{r}{q}\nabla_\theta\right)\partial_\parallel \tilde{T}_e \\ &+\frac{1}{\omega_{cy}}\frac{1}{\rho^{\mathrm{eq}}}\left[J_\zeta^{\mathrm{eq}}\partial_\parallel \tilde{T}_e + \frac{2}{3}(1+\alpha)\,T_e^{\mathrm{eq}}\partial_\parallel \tilde{J}_\zeta - \frac{2}{3}\frac{1}{\rho^{\mathrm{eq}}}J_\zeta^{\mathrm{eq}}T_e^{\mathrm{eq}}\partial_\parallel \tilde{\rho}\right], \end{aligned} \tag{40}$$

and where

$$U^{t+\Delta t} = \nabla\cdot(\rho_{00}^t\,\nabla\Phi^{t+\Delta t}), \tag{41a}$$

$$\partial_\parallel \tilde{f} = \left(\frac{\partial}{\partial\zeta} - \frac{r}{q}\nabla_\theta\right)\tilde{f} - \frac{df^{\mathrm{eq}}}{dr}\nabla_\theta \tilde{\Psi}, \tag{41b}$$

where S_1 to S_4 is the right side of Eqs. (31) to (34), evaluated at t instead of $t+\Delta t/2$.

The equations in (36) are solved as a block-tridiagonal system. Since only linear terms are treated implicitly and since the geometry is cylindrical, the matrix does not couple the terms in Eq. (3) that have different (m, n) values. The variables Φ, ρ, Ψ, T_e, and U are included in the solution vector to get a solvable system. When diamagnetic and thermal force effects are not included in the equations, the sine and cosine terms decouple, and the representation can be simplified by taking only cosine terms in Ψ, ρ, and T_e and sine terms in Φ and U, giving 5×5 block matrices. When these effects are included, the blocks become 10×10. The number of such blocks on the main diagonal is given by the number of grid points in the radial direction. This finite matrix problem is solved with the routine BTMS [15].

The parameter W in Eq. (36) is set to $\frac{1}{2}$ for linear problems, making the scheme second-order accurate in time. When the timestep is of the order of the inverse of the eigenvalue, the resulting time evolution cannot be considered a solution of the initial value problem. However, as has been shown in [16], the implicit method becomes an iteration scheme for solving the eigenvalue problem with Δt interpreted as the convergence parameter. Convergence to the linear solution is very rapid.

magnitude of the eigenvalue, allowing very rapid convergence. Conversely, for nonlinear problems we are mainly interested in the time evolution. In this case, $\Delta t = 10^{-2}/\max(\gamma, \omega_r)$ is chosen for the initial timestep. Subsequent evolution requires reduction of the timestep due to changes in instantaneous growth rates and frequencies and the effects of nonlinear terms. W is usually set to 1 for nonlinear problems since this choice allows for larger timesteps. Since the nonlinear terms are, in any case, only first-order accurate in time, there is little reason to make the linear terms more accurate.

3.3. *Comparison of Schemes*

For linear calculations the convergence parameter is only limited by the magnitude of the eigenvalue, so the implicit scheme always converges more rapidly than the mostly-explicit scheme. Although the mostly-explicit method is faster per step, stability constraints require a small timestep that leads to a large number of steps for convergence. There is no noticeable difference between the converged growth rates and eigenfunctions obtained with both methods. In addition, as an iterative method, the implicit scheme can be used to obtain not only the fastest growing mode, but also the spectrum of unstable eigenvalues and eigenfunctions by varying the convergence parameter Δt. Both facts make the implicit method more convenient for linear calculations.

In the case of nonlinear calculations, the relative efficiency of schemes depends on the size of the nonlinear terms. Therefore, the efficiency depends on the problem being studied. However, the results themselves are independent of the scheme used. We next discuss three different calculations that typify different regions of efficiency for the two numerical schemes:

1. *Disruption studies.* These calculations involve the nonlinear interaction of low-m tearing modes of different helicities. During the initial phase of the calculation, the spectrum is clearly dominated by the very low-m linearly unstable tearing modes ($m = 2$ and $m = 3$) with large amplitudes ($\tilde{B}/B_0$ of a few percent). The evolution of the ($m = 2$; $n = 1$) mode is practically the same as in the case of single-helicity, while the ($m = 3$, $n = 2$) mode shows a strong destabilization, in agreement with analytical predictions [17, 18]. Later in the calculation, an explosive growth involving many modes is observed. This is a physical effect, as has been shown in analytic studies [8] and by performing the calculation with different schemes. The nonlinear terms dominate over the linear terms during much of the calculation. As the size of the nonlinear terms increases, the timestep for the implicit scheme must be reduced. When the nonlinear terms dominate, the timestep of the implicit scheme is limited to a value similar to the one used in the explicit scheme. Since the time to calculate a step with the implicit scheme is, for a run using 106 modes, about three times larger than for the explicit scheme, the latter becomes more efficient. This ratio changes with the number of modes included in the calculation and is less severe for higher numbers of modes when the relative computational time spent in convolutions is larger; it always, however, favors the explicit scheme. The results

themselves do not depend on the numerical scheme employed. Only when one looks at details, such as the total cumulative energy-balance error ΔE_T defined in Eq. (24), can one observe some differences because the mostly-implicit scheme is Δt accurate, while the mostly-explicit scheme is Δt^2 accurate. Comparisons of results from the two methods are shown in the next section.

2. *Calculations of turbulence at the tokamak edge.* The model used in this type of calculation is based on the nonlinear evolution of rippling modes of different helicities. A saturated, turbulent, steady state situation is obtained. The level of saturation of these resistivity-driven modes is low ($\tilde{B}/B_0$ on the order of 10^{-4}). Thus, the linear terms dominate over the nonlinear terms throughout the calculation. Consequently, the implicit scheme timestep is essentially limited by the fastest growing mode. In contrast to the disruptive cases, the basic effect of the high-m turbulence is to stabilize the low-m modes and to cause the saturation. This phenomenon has been studied in detail in [7] and carefully tested numerically. Increasing the number of high-m modes, and, as a consequence, the number of nonlinear couplings, leads to a saturated state without the need of strongly decreasing the timestep in the implicit method. The timestep needed using the explicit method for the same type of calculation is much smaller due to stability requirements, but, as in the case of tearing modes, the results obtained are the same. The difference in timestep is more pronounced for higher values of S and $\chi_\parallel$. Figure 1 compares the change in the timestep Δt during computations using the mostly-implicit and mostly-explicit schemes. The timestep comparison is for a calculation with 49 modes,

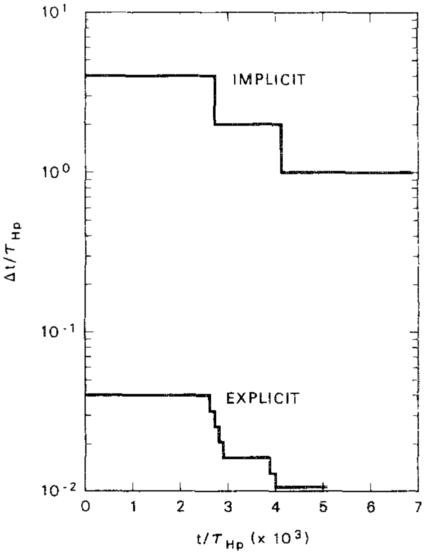

FIG. 1. Change in the timestep Δt during the evolution for computations of resistivity-driven turbulence using the mostly-implicit and mostly-explicit schemes. The time to calculate a step with the implicit scheme is about four times larger than for the explicit-scheme for this case.

227 grid points, and with the physical parameter $q = 1 + (r/0.632)^2$, $S = 10^5$, and $\bar{\chi}_\parallel = 2.5$. The initial ratio between timesteps is 100 and remains practically the same during the whole evolution. The mostly-explicit scheme is only four times faster in number of steps per unit of computational time. This makes the mostly-implicit scheme about 25 times faster than the mostly-explicit one and, therefore, more efficient for this type of calculation. This saving in computational time allows us to carry out calculations including up to 200 modes and 200 grid points, which is the limit set by the memory size of our present computer. This calculation would be impossible to perform in a reasonable amount of time using the mostly-explicit scheme.

3. *Drift-tearing modes.* When diamagnetic effects are included in the calculation, ω_{*e}^{-1} becomes the shortest timescale for realistic parameter values. Due to this, the timestep is severely reduced for the mostly-explicit scheme. However, the dependence on ω_{*e} is much weaker for the mostly-implicit scheme. This makes, in general, the mostly-implicit scheme more appropriate at the beginning of the computation. However, due to nonlinear effects, the timestep corresponding to the mostly-implicit scheme must be reduced faster than in the mostly-explicit case, reaching a point when the mostly-implicit scheme is no longer more economical

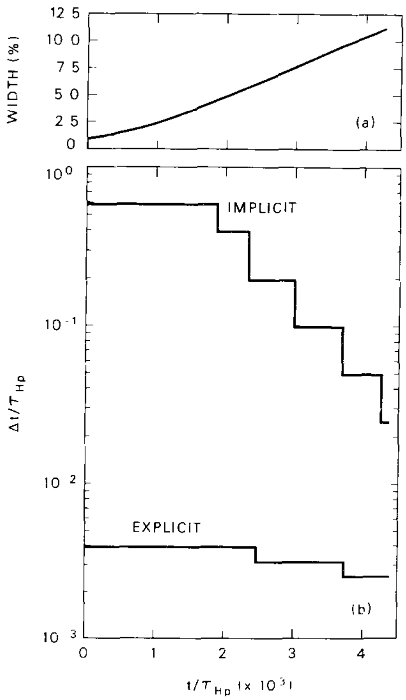

FIG. 2. Change in the timestep Δt during single-helicity computations of drift-tearing modes using the mostly-implicit and mostly-explicit schemes. The ratio of computational time per step between both schemes is about ten. The island width evolution is also shown.

than the mostly-explicit one. This is the case for moderate ω_{*e} values ($\omega_r \lesssim 10\gamma$) when the mostly-implicit scheme is more efficient at the beginning of the computation, but the ratio between timesteps is < 100. Using both numerical schemes, we have calculated the nonlinear single-helicity evolution of the $m=2$, $n=1$ drift-tearing mode. Thermal force effects were also included in these calculations. The equilibrium is characterized by $q = 1.08[1+(r/0.53)^4]^{1/2}$, $S = 8.85 \times 10^5$, $\bar{\chi}_{\parallel} = 11.56$, and $\omega_{*e} = 1.2 \times 10^{-3}$. This corresponds to a toroidal field of 9 kG, central peak ion density of 7×10^{13} cm^{-3}, and central electron temperature of 240 eV. Six modes and 280 grid points were used. The comparison of the timestep evolution for this calculation is shown in Fig. 2. At the beginning of the computation, the timestep for the mostly-implicit sheme is 100 times larger than for the mostly-explicit case, but this factor is reduced to < 10 when the island width is $\sim 11\%$, at which point the mostly-implict scheme is no longer the most economical since the computational time per step in the implicit method is a factor of ten larger than for the mostly-explicit scheme. The overall calculation time is optimized by switching from the implicit to the explicit scheme at the appropriate time.

4. NUMERICAL CONVERGENCE

In these calculations, there are five possible sources of numerical error:

1. roundoff,
2. numerical instability,
3. truncation error due to finite timestep (Δt truncation),
4. truncation error due to a finite spectrum of modes (mode truncation), and
5. truncation error due to finite grid in r (Δr truncation).

These sources of error have been discussed in detail in [4].

These calculations have been performed on a CRAY-1 computer, one that the floating point format provides a 48-bit (14+ decimal-digit) mantissa. A compiler option exists that implements lower accuracy arithmetic. Calculations using 36-bit [illegible]

If the timestep is too large, a numerical instability grows rapidly. Such an instability is easily identified by its rapid growth, as well as its nonphysical shape. The timestep control procedure searches for these numerical instabilities and, when one is detected, reduces the timestep to stabilize it [3, 4].

To investigate the role of Δt truncation, two disruption calculations (Fig. 3) are compared. In each case, the magnetic energy (E_{M}) curves agree, but some effects can be seen in ΔE_{T}. The mostly-implicit integrator is order Δt accurate, compared with the mostly-explicit integrator that is order Δt^2, and, thus, the former yields a somewhat larger value of ΔE_{T} since it contains more Δt truncation error. But the fact is that the solution itself is not sensitive to the choice of scheme.

It is especially interesting to compare the different physics calculations discussed

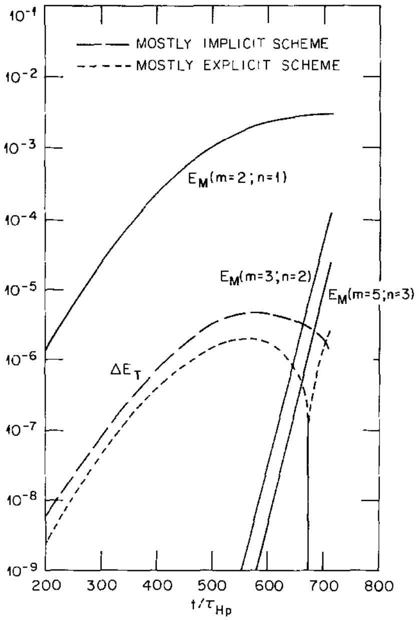

FIG. 3. The time history of Δt truncation error ΔE_T for two disruption calculations with 200 grid points and 11 modes, using the mostly-implicit and mostly-explicit schemes. The value of S is 10^5. The equilibrium is characterized by a q-profile $q = 1.344[1 + (r/0.56)^{6.48}]^{1/3.24}$. The solutions, as can be seen from the time history of the magnetic energies of the three largest modes $E_M(2; 1)$, $E_M(3; 2)$, and $E_M(5; 3)$ are the same for both calculations. The timestep used in both methods is the same, and changes from 7.6×10^{-5} to $2.5 \times 10^{-5}\, \tau_{Hp}$ during the evolution.

in the previous section. Due to the opposite dynamical effects of the turbulent background on the stability of the low-m modes, the comparison of the mode spectrum convergence is of particular interest. Two different convergence studies are shown here. The numerical scheme used in each one is the appropriate one for the type of calculation. However, the results are independent of the choice of scheme, and the particular choice is determined only on the basis of efficiency. Consider first the case of a multiple-helicity tearing mode calculation modeling a tokamak disruption. For the particular case presented here, the equilibrium is characterized by a q-profile $q = 1.344[1 + (r/0.65)^{6.48}]^{1/3.24}$. The value of S considered is 10^5. The equilibrium is linearly unstable to the ($m = 2$; $n = 1$) and ($m = 3$; $n = 2$) tearing modes. Both modes are initially perturbed with initial island widths $W^I_{2,1} = 10^{-2}$, $W^I_{3,2} = 10^{-3}$. Details on the results of this calculation have been reported elsewhere [4]. Here, we will concentrate on the convergence studies with respect to number of modes. In Fig. 4(a) the magnetic energy of the dominant mode ($m = 2$; $n = 1$) is plotted as a function of time when 11, 48, 106, and 191 modes are included in the calculation. The number of radial grid points is 200 for each case. The total cumulative energy-balance error ΔE_T is similar for the four cases, growing to only 10^{-4} at the end of the calculation. A strong destabilization effect is observed when

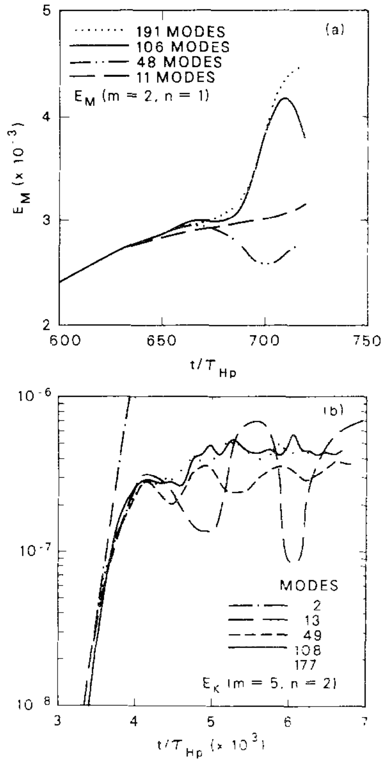

FIG. 4. Evolution of the $(m=2;\ n=1)$ magnetic energy for a multiple-helicity tearing mode calculation and the $(m=5;\ n=2)$ kinetic energy for a multiple-helicity rippling mode calculation where different numbers of modes are included in the computations. The number of grid points is 200 in the first case and 227 in the second.

we increase the number of modes, in agreement with a proposed analytical model [8]. This destabilization cannot be seen when 11 or 48 modes are included in the computation. Moreover, the destabilization is stronger when 191 modes are included, suggesting that additional modes would be still more destabilizing. This is consistent with the fact that the destabilization mechanism is due to the high-m turbulence. Converged results can be obtained with present calculations up to a certain time $t \sim 700\tau_{Hp}$ for the case shown in Fig. 4(a). To try to go further in time requires more modes than our present computer storage permits.

A similar convergence study is shown for a case of resistivity-driven turbulence in Fig. 4(b). As this process is dominantly electrostatic, the kinetic energy is the relevant diagnostic. The dominant mode is the $(m=5;\ n=2)$, and the average resistivity profile is held constant in time in such a way that saturation can be reached only by nonlinear effects (no quasi-linear saturation) [7]. This procedure can be physically justified by the balance of ohmic heating and thermal diffusion in the experiment. The equilibrium is characterized by a q-profile $q = 1 + (r/0.632)^2$,

$S = 10^5$, and $\bar{\chi}_{\|} = 2.5$. All the modes present in the calculation are initially perturbed using Eq. (11) with $W^I = 10^{-5}$. It is clear that at least 49 modes are needed to reach saturation, and reasonable converged results are obtained with 108 modes. Here, we use a radial grid of 227 points, most of them concentrated in the region $0.7 < r < 1$. The 49 mode case is the same as the one referred to in Fig. 1.

Three main conclusions can be extracted from these studies. First, the destabilizing or stabilizing effect observed when more modes are added is due to the particular dynamics of the problem and not to the numerical scheme. To get a reliable result, a careful convergence analysis with respect to the number of modes is always needed. Second, the choice of scheme is given by the level of turbulence in each particular case, which reflects the dominance of linear or nonlinear terms during the calculation. Third, full nonlinear 3D calculations can be carried out at present for only a limited set of parameters. More storage is needed to expand the region in which these calculations can be performed.

Finally, Fig. 5 shows convergence studies with respect to the number of radial grid points. The physical parameters for the cases shown are the same as the ones

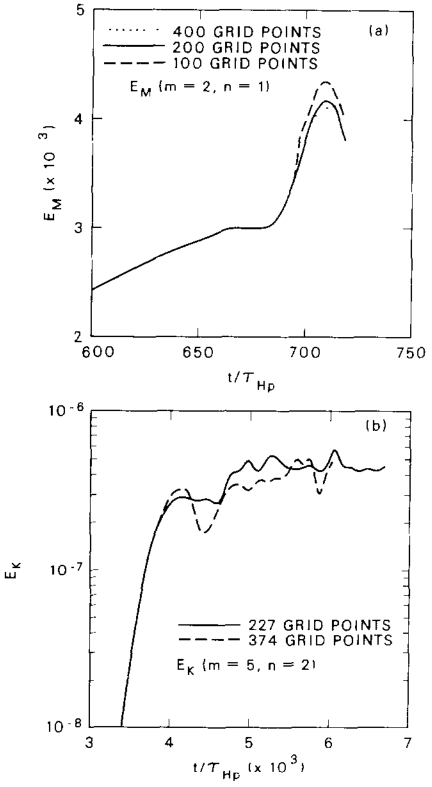

FIG. 5. The same as Fig. 4, varying the number of radial grid points used in the computations. The number of modes included is 106 in the first case and 108 in the second.

used in the mode convergence studies. The number of modes included is 106 for the tearing mode calculations and 108 for the rippling mode calculations, since it is clear from the mode convergence studies that reasonable converged results are obtained with these sets of modes. It is apparent that, for the disruption calculation, even 100 grid points are enough to show destabilization. However, for the case of resistivity-driven turbulence, the calculation cannot be carried out with <200 grid points because of the radial localization of the modes. The differences are much smaller than in the case of mode convergence.

5. CONCLUSIONS

Two different time integration schemes are used to solve a reduced set of resistive MHD equations, including diamagnetic and thermal force effects. The mostly-explicit scheme is second-order accurate in time and is explicit, except for convective and perpendicular diffusive terms, while the mostly-implicit scheme is first-order accurate in time and is fully implicit for linear terms and explicit for nonlinear terms. Both schemes use a Fourier representation in the angular variables and finite difference in the radial coordinate. The solutions obtained from the two schemes are the same and differ only in efficiency.

The mostly-implicit scheme is always more efficient for linear calculations. The relative efficiency of both schemes for nonlinear calculations depends on the problem being studied. For cases where the nonlinear terms dominate over the linear terms early in the calculation, like the nonlinear interaction of tearing modes, the explicit scheme is, in general, more efficient. Conversely, the implicit scheme is more efficient in cases where the linear terms dominate over the nonlinear terms during the whole evolution, reaching a saturated steady state, like the nonlinear evolution of rippling modes. Finally, there are some cases in which the implicit scheme is more appropriate at the beginning of the calculation, but at some time during the evolution, the nonlinear terms dominate over the linear ones, making it advantageous to switch to the explicit scheme during the calculation.

Convergence studies with respect to the number of radial grid points and with respect to the number of modes included in the computations are needed to verify the solution. Both tearing mode driven disruption calculations and saturated rippling mode calculations require a large numbe of modes. The addition of modes to the representation in the tearing mode disruption increases the level of destabilization. It can be seen that this is not a characteristic of the numerical scheme since the addition of modes to the rippling mode calculation provides additional stabilization and, ultimately, a converged solution. The different behavior is due to the basic dynamics of the problem, not to the numerical implementation.

ACKNOWLEDGMENTS

This research was sponsored by the Office of Fusion Energy, U.S. Department of Energy, under Contract DE-AC05-84OR21400 with Martin Marietta Energy Systems, Inc.

REFERENCES

1. H. R. STRAUSS, *Phys. Fluids* **19** (1976), 134.
2. N. R. SAUTHOFF, S. VON GOELER, AND W. STODIEK, *Nucl. Fusion* **18** (1978), 1445.
3. H. R. HICKS, B. A. CARRERAS, J. A. HOLMES, D. K. LEE, AND B. V. WADDELL, *J. Comput. Phys.* **44** (1981), 46; Erratum, *J. Comput. Phys.* **53** (1984), 205.
4. H. R. HICKS, B. A. CARRERAS, L. GARCIA, AND J. A. HOLMES, "The Reliability of Initial-Value MHD Calculations of Tokamak Disruptions," ORNL/TM – 9127, June, 1984; H. R. HICKS, B. A. CARRERAS, AND J. A. HOLMES, *J. Comput. Phys.* **60** (1985), 588.
5. H. R. HICKS, B. A. CARRERAS, AND J. A. HOLMES, *Phys. Fluids* **27**, 909 (1984).
6. J. F. DRAKE, T. M. ANTONSEN, JR., A. B. HASSAM, AND N. T. GLADD, *Phys. Fluids* **26** (1983), 2509.
7. L. GARCIA, P. H. DIAMOND, B. A. CARRERAS, AND J. D. CALLEN, *Phys. Fluids* **28** (1985), 2147.
8. P. H. DIAMOND, R. D. HAZELTINE, Z. G. AN, B. A. CARRERAS, AND H. R. HICKS, *Phys. Fluids* **27** (1984), 1449.
9. J. W. EASTWOOD AND K. I. HOPCRAFT, *Bull. Amer. Phys. Soc.* **28** (1983), 1207.
10. D. BISKAMP, *Nucl. Fusion* **18** (1978), 1059.
11. D. A. MONTICELLO AND R. B. WHITE, *Phys. Fluids* **23** (1980), 366.
12. S. I. BRAGINSKII, "Transport Processes in a Plasma," *Reviews of Plasma Physics*, Vol. I, edited by M. A. Leontovich, (Consultants Bureau, New York, 1965), p. 205.
13. B. V. WADDELL, B. A. CARRERAS, H. R. HICKS, AND J. A. HOLMES, *Phys. Fluids* **22** (1979), 896.
14. B. A. CARRERAS, P. W. GAFFNEY, H. R. HICKS, AND J. D. CALLEN, *Phys. Fluids* **25** (1982), 1231.
15. A. C. HINDMARSH, "Solution of Block-Tridiagonal Systems of Algebraic Equations," UCID-30150, 1977 (unpublished).
16. L. A. CHARLTON, J. A. HOLMES, H. R. HICKS, V. E. LYNCH, AND B. A. CARRERAS, *J. Comput. Phys.* **63** (1986), 107.
17. B. A. CARRERAS, M. N. ROSENBLUTH, AND H. R. HICKS, *Phys. Rev. Lett.* **46** (1981), 1131.
18. R. G. KLEVA, J. F. DRAKE, AND A. BONDESON, *Phys. Fluids* **27** (1984), 769.